COMMUNICATIONS IN NUMERICAL METHODS IN ENGINEERING
Commun. Numer. Meth. Engng (2009)
Published online in Wiley InterScience (www.interscience.wiley.com). DOI: 10.1002/cnm.1291

Adaptive analysis using the node-based smoothed finite element method (NS-FEM)

T. Nguyen-Thoi[1,3,*,†], G. R. Liu[1,2], H. Nguyen-Xuan[2,3] and C. Nguyen-Tran[3]

[1]*Center for Advanced Computations in Engineering Science (ACES), Department of Mechanical Engineering, National University of Singapore, 9 Engineering Drive 1, Singapore 117576, Singapore*
[2]*Singapore-MIT Alliance (SMA), E4-04-10, 4 Engineering Drive 3, Singapore, 117576, Singapore*
[3]*Department of Mathematics and Computer Science, University of Natural Sciences, Vietnam National University—HCM, Vietnam*

SUMMARY

The paper presents an adaptive analysis within the framework of the node-based smoothed finite element method (NS-FEM) using triangular elements. An error indicator based on the recovery strain is used and shown to be asymptotically exact by an effectivity index and numerical results. A simple refinement strategy using the newest node bisection is briefly presented. The numerical results of some benchmark problems show that the present adaptive procedure can accurately catch the appearance of the steep gradient of stresses and the occurrence of refinement is concentrated properly. The energy error norms of adaptive models for both NS-FEM and FEM obtain higher convergence rate compared with the uniformly refined models, but the results of NS-FEM are better and achieve higher convergence rate than those of FEM. The effectivity index of NS-FEM is also closer and approaches to unity faster than that of FEM. The upper bound property in the strain energy of NS-FEM is always verified during the adaptive procedure.

Received 21 October 2008; Revised 11 April 2009; Accepted 22 May 2009

KEY WORDS: finite element method (FEM); meshfree methods; node-based smoothed finite element method (NS-FEM); upper bound; error indicator; adaptive analysis

1. INTRODUCTION

Adaptive analysis has been used in the traditional finite element method (FEM) and various procedures for error estimate and refinement have been developed. Among error estimators, residual-based and recovery-based ones are the most popular. The residual-based error estimators have

*Correspondence to: T. Nguyen-Thoi, Center for Advanced Computations in Engineering Science (ACES), Department of Mechanical Engineering, National University of Singapore, 9 Engineering Drive 1, Singapore 117576, Singapore.
†E-mail: g0500347@nus.edu.sg, thoitrung76@yahoo.com

been developed by considering local residuals of the numerical solutions, in a patch of elements or in a single element. This type of error estimators was originally introduced by Babuska and Rheinboldt [1, 2], and then developed by many others researchers such as Bank and Weiser [3], Ainsworth and Oden [4, 5]. Recovery-based error estimators have been studied by using of the recovery solutions derived from *a posteriori* treatment of the numerical results to obtain more accurate representation of the unknowns. This type of error estimators was introduced and developed by Zienkiewicz and Zhu [6–8] and has been widely used in the FEM. In addition, error estimators based on the construction of a statically admissible stress field were also introduced by Ladevèze [9–11]. Once the error estimator process has been set up, it is natural to seek a refinement scheme by which the design can be improved. There are various procedures of the refinement and they may be broadly classified into three categories: h-type refinement, p-type refinement and r-type refinement [12, 13]. In an h-type refinement, the same class of elements will continue to be used but more elements are needed at the necessary positions to provide maximum economy in reaching the desired solution. In a p-type refinement, the same elements are used but the order of the polynomial functions is increased. In a r-type refinement, the nodes of elements are relocated but the mesh connectivity is kept unchanged [13]. Recently, an e-type refinement (*enrichment* adaptivity) that uses an extended global derivative recovery for enriched FEMs such as extended finite element method (XFEM) is also proposed [14–17]. The e-type refinement is shown to be simple and suitable to industrial applications.

In the other front of development of numerical methods, a conforming nodal integration technique has been proposed by Chen *et al.* [18] to stabilize the solutions in the context of the meshfree method and then applied in the natural-element method [19]. Liu *et al.* have applied this technique to formulate the linear conforming point interpolation method (LC-PIM) [20] and the linearly conforming radial point interpolation method [21]. Applying the same idea to the FEM, an element-based smoothed finite element method (CS-FEM or SFEM) [22–25], and node-based smoothed finite element method (NS-FEM) [24] have also been formulated.

In the CS-FEM, the strain smoothing operation and the integration of the weak form are performed over smoothing cells (SCs) located inside the quadrilateral elements, as shown in Figure 1. The CS-FEM has been developed for general n-sided polygonal elements [26], dynamic analyses [27], incompressible materials using selective integration [28, 29], and further extended for plate and shell analyses [30–34], respectively. In addition, CS-FEM has also been coupled to the XFEM [35] to solve fracture mechanics problems in 2D continuum and plates [36].

In the NS-FEM, the strain smoothing operation and the integration of the weak form are performed over the smoothing cells associated with nodes, and methods can be applied easily to triangular, 4-node quadrilateral, n-sided polygonal elements for 2D problems and tetrahedral elements for 3D problems. For n-sided polygonal elements, the cell $\Omega^{(k)}$ associated with the node k is created by connecting sequentially the mid-edge-point to the central points of the surrounding n-sided polygonal elements of the node k as shown in Figure 2. When only linear triangular or tetrahedral elements are used, the NS-FEM produces the same results as the method proposed by Dohrmann *et al.* [37] or to the LC-PIM by Liu *et al.* [20] using linear interpolation. Liu and Zhang [38] have provided an intuitive explanation and showed numerically that the LC-PIM can produce an upper bound to the exact solution in the strain energy, when a reasonably fine mesh is used. The upper bound property was also found in the NS-FEM by Liu *et al.* [24]. Both upper and lower bounds in the strain energy for elastic solid mechanics problems can now be obtained by combining the NS-FEM with the CS-FEM (for n-sided polygonal elements) or with the FEM (for triangular or 4-node quadrilateral elements). Further developed, a nearly exact solution in strain

DOI: 10.1002/cnm

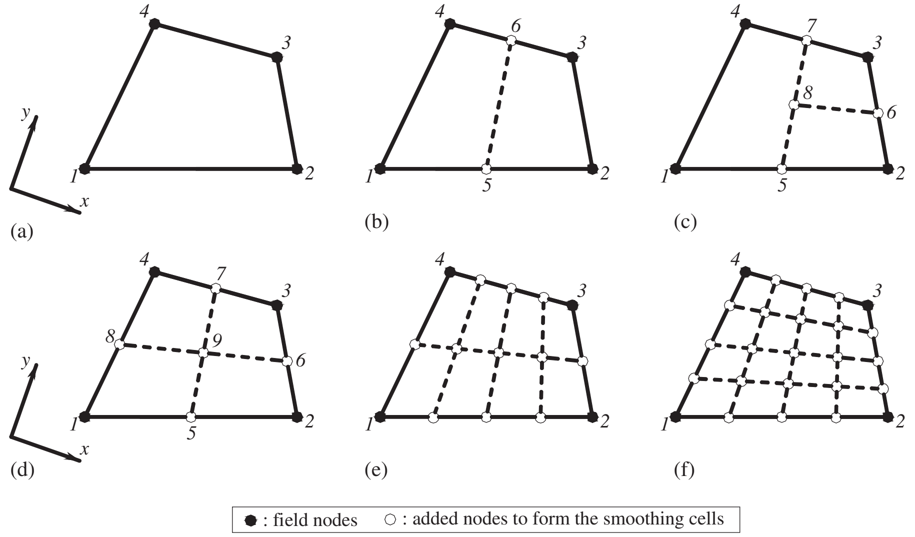

Figure 1. Division of quadrilateral element into the smoothing cells (SCs) in CS-FEM by connecting the mid-edge-points of opposite edges of smoothing cells: (a) 1 SC; (b) 2 SCs; (c) 3 SCs; (d) 4 SCs; (e) 8 SCs; and (f) 16 SCs.

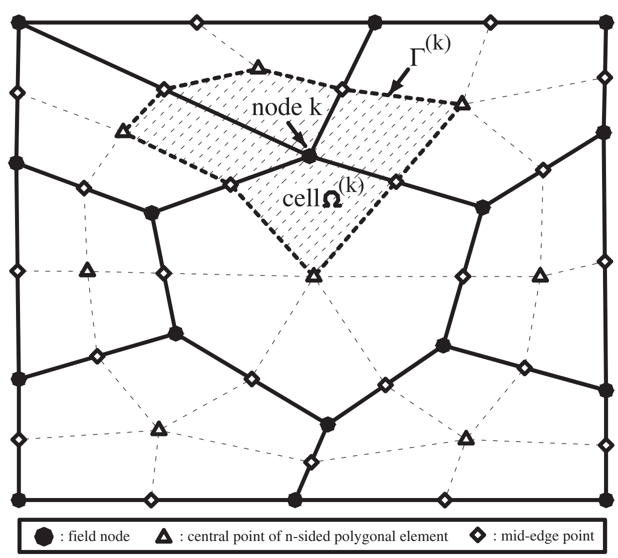

Figure 2. n-sided polygonal elements and the smoothing cell (shaded area) associated with nodes in the NS-FEM.

energy using triangular and tetrahedral elements is also proposed by Liu *et al.* [39] by combining a scale factor $\alpha \in [0, 1]$ with the NS-FEM and the FEM to give a so-called the alpha finite element method (αFEM).

DOI: 10.1002/cnm

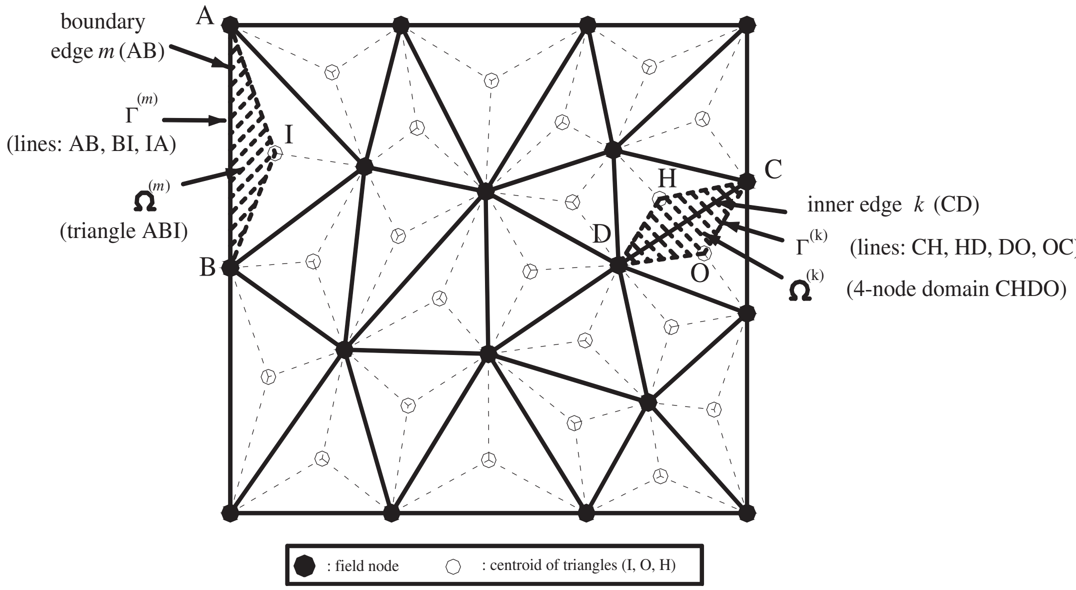

Figure 3. Triangular elements and the smoothing domains (shaded areas) associated with edges in the ES-FEM.

Besides the upper bound property in the strain energy, the NS-FEM also possesses the others interesting properties: (i) it is immune from the volumetric locking; (ii) it allows the use of polygonal elements with an arbitrary number of sides [24]. In the NS-FEM, the integration on the smoothing domains is transformed to line integrations along the edges of the SC and such an integration can be evaluated using directly the values of shape functions (not their derivatives).

Recently, an edge-based smoothed finite element method (ES-FEM) was also been formulated by Liu *et al.* [40] for static, free and forced vibration analyses in 2D problems. The ES-FEM uses triangular elements that can be generated automatically for complicated domains. In the ES-FEM, the system stiffness matrix is computed using strains smoothed over the smoothing domains associated with the edges of the triangles. For triangular elements, the smoothing domain $\Omega^{(k)}$ associated with the edge k is created by connecting two endpoints of the edge to the centroids of adjacent elements as shown in Figure 3. In addition, the idea of the ES-FEM is quite straightforward to extend for the n-sided polygonal elements [41] and for the 3D problems using tetrahedral elements to give a so-called the face-based smoothed finite element method [42]. ES-FEM has been developed for 2D piezoelectric analysis [43].

The objective of the present work is to develop an effective adaptive procedure for NS-FEM using triangular elements. An error indicator based on the recovery strain is proposed and a simple refinement strategy using the newest node bisection is also briefly presented. An effectivity index and numerical results are provided to show that the error indicator proposed is asymptotically exact, and the recovery strain is a reliable representation of the analytical strain, especially for the highly singular problems.

The paper is outlined as follows. In Section 2, the idea of the NS-FEM based on triangle elements is briefly presented. An adaptive procedure including an error indicator based on the

DOI: 10.1002/cnm

recovery strain and a simple refinement strategy is described in Section 3. In Section 4, some numerical examples are conducted and discussed to demonstrate the effectiveness of the proposed adaptive procedure. Some concluding remarks are made in Section 5.

2. BRIEFING ON THE NS-FEM BASED ON TRIANGULAR ELEMENTS (NS-FEM-T3)

2.1. Briefing on the finite element method (FEM) [12, 44, 45]

The discrete equations of the FEM are derived from the Galerkin weak form and the integration is performed on the basis of element as follows:

$$\int_{\Omega} (\nabla_s \delta \mathbf{u})^{\mathrm{T}} \mathbf{D} (\nabla_s \mathbf{u}) \, \mathrm{d}\Omega - \int_{\Omega} \delta \mathbf{u}^{\mathrm{T}} \mathbf{b} \, \mathrm{d}\Omega - \int_{\Gamma_t} \delta \mathbf{u}^{\mathrm{T}} \bar{\mathbf{t}} \, \mathrm{d}\Gamma = 0 \tag{1}$$

where $\mathbf{b}$ is the vector of external body forces, $\mathbf{D}$ is a symmetric positive-definite matrix of material constants, $\bar{\mathbf{t}}$ is the prescribed traction vector on the natural boundary Γ_t, $\mathbf{u}$ is trial functions, $\delta\mathbf{u}$ is test functions and $\nabla_s \mathbf{u}$ is the symmetric gradient of the displacement field.

The FEM uses the following trial and test functions:

$$\mathbf{u}^h(\mathbf{x}) = \sum_{I=1}^{N_n} \mathbf{N}_I(\mathbf{x}) \mathbf{d}_I, \quad \delta \mathbf{u}^h(\mathbf{x}) = \sum_{I=1}^{N_n} \mathbf{N}_I(\mathbf{x}) \delta \mathbf{d}_I \tag{2}$$

where N_n is the total number of nodes of the problem domain, $\mathbf{d}_I$ is the nodal displacement vector and $\mathbf{N}_I(\mathbf{x})$ is a matrix of shape functions of Ith node.

By substituting the approximations, $\mathbf{u}^h$ and $\delta\mathbf{u}^h$, into the weak form and invoking the arbitrariness of virtual nodal displacements, Equation (1) yields the discretized system of algebraic equations

$$\mathbf{K}^{\mathrm{FEM}} \mathbf{d} = \mathbf{f} \tag{3}$$

where $\mathbf{K}^{\mathrm{FEM}}$ is the system stiffness matrix, $\mathbf{f}$ is the element force vector that are assembled with entries of

$$\mathbf{K}_{IJ}^{\mathrm{FEM}} = \int_{\Omega_e} \mathbf{B}_I^{\mathrm{T}} \mathbf{D} \mathbf{B}_J \, \mathrm{d}\Omega \tag{4}$$

$$\mathbf{f}_I = \int_{\Omega_e} \mathbf{N}_I^{\mathrm{T}}(\mathbf{x}) \mathbf{b} \, \mathrm{d}\Omega + \int_{\Gamma_t} \mathbf{N}_I^{\mathrm{T}}(\mathbf{x}) \bar{\mathbf{t}} \, \mathrm{d}\Gamma \tag{5}$$

In Equation (4), the *strain gradient matrix* is defined as

$$\mathbf{B}_I(\mathbf{x}) = \nabla_s \mathbf{N}_I(\mathbf{x}) \tag{6}$$

that produces *compatible* strain fields. Using the triangular elements with the linear shape functions, the strain gradient matrix $\mathbf{B}_I(\mathbf{x})$ contains only constant entries. Equation (4) then becomes

$$\mathbf{K}_{IJ}^{\mathrm{FEM}} = \mathbf{B}_I^{\mathrm{T}} \mathbf{D} \mathbf{B}_J A_e \tag{7}$$

where $A_e = \int_{\Omega_e} \mathrm{d}\Omega$ is the area of the element.

DOI: 10.1002/cnm

2.2. The NS-FEM based on triangular elements (*NS-FEM-T3*)

The NS-FEM works for polygonal elements of arbitrary sides [24]. Here we brief only the formulation for triangular element (NS-FEM-T3).

Similar to the FEM, the NS-FEM also uses a mesh of elements. When 3-node triangular elements are used, the shape functions used in the NS-FEM-T3 are also identical to those in the FEM-T3, and hence the displacement field in the NS-FEM-T3 is also ensured to be continuous on the whole problem domain. However, being different from the FEM-T3, which performs the integration required in the weak form (1) on the elements, NS-FEM-T3 performs such the integration based on the nodes, and strain smoothing technique [18] is used. In such a nodal integration process, the problem domain Ω is divided into N_n smoothing cells $\Omega^{(k)}$ associated with nodes k such that $\Omega=\sum_{k=1}^{N_n}\Omega^{(k)}$ and $\Omega^{(i)}\cap\Omega^{(j)}=\oslash$, $i\neq j$, in which N_n is the total number of field nodes located in the entire problem domain. For triangular elements, the cell $\Omega^{(k)}$ associated with the node k is created by connecting sequentially the mid-edge-points to the centroids of the surrounding triangular elements of the node k as shown in Figure 4. As a result, each triangular element will be divided into three quadrilateral sub-domains and each quadrilateral sub-domain is attached with the nearest field node. The cell $\Omega^{(k)}$ associated with the node k is then created by combination of each nearest quadrilateral sub-domain of all elements surrounding the node k.

Applying the node-based smoothing operation, the *compatible* strains $\boldsymbol{\varepsilon}=\nabla_s\mathbf{u}$ in Equation (1) is used to create a *smoothed* strain on the cell $\Omega^{(k)}$ associated with node k

$$\tilde{\boldsymbol{\varepsilon}}_k=\int_{\Omega^{(k)}}\boldsymbol{\varepsilon}(\mathbf{x})\Phi_k(\mathbf{x})\,\mathrm{d}\Omega=\int_{\Omega^{(k)}}\nabla_s\mathbf{u}(\mathbf{x})\Phi_k(\mathbf{x})\,\mathrm{d}\Omega \tag{8}$$

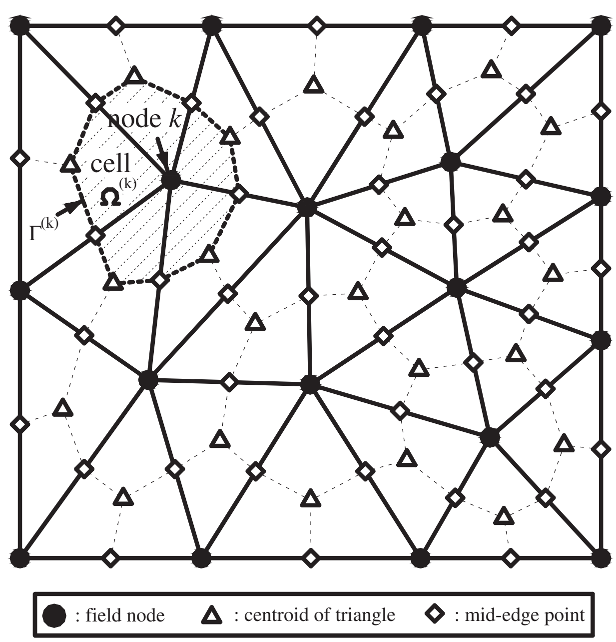

Figure 4. Triangular elements and smoothing cells (shaded area) associated with the nodes in the NS-FEM.

DOI: 10.1002/cnm

where $\Phi_k(\mathbf{x})$ is a given smoothing function that satisfies at least unity property

$$\int_{\Omega^{(k)}} \Phi_k(\mathbf{x})\,\mathrm{d}\Omega = 1 \tag{9}$$

Using the following constant smoothing function:

$$\Phi_k(\mathbf{x}) = \begin{cases} 1/A^{(k)}, & \mathbf{x} \in \Omega^{(k)} \\ 0, & \mathbf{x} \notin \Omega^{(k)} \end{cases} \tag{10}$$

where $A^{(k)} = \int_{\Omega^{(k)}} \mathrm{d}\Omega$ is the area of the cell $\Omega^{(k)}$ and applying a divergence theorem, one can obtain the smoothed strain that is constant over the domain $\Omega^{(k)}$ as follows:

$$\tilde{\boldsymbol{\varepsilon}}_k = \frac{1}{A^{(k)}} \int_{\Gamma^{(k)}} \mathbf{u}(\mathbf{x})\mathbf{n}^{(k)}(\mathbf{x})\,\mathrm{d}\Gamma \tag{11}$$

where $\Gamma^{(k)}$ is the boundary of the domain $\Omega^{(k)}$ as shown in Figure 4, and $\mathbf{n}^{(k)}(\mathbf{x})$ is the outward normal vector matrix on the boundary $\Gamma^{(k)}$ and has the form

$$\mathbf{n}^{(k)}(\mathbf{x}) = \begin{bmatrix} n_x^{(k)} & 0 \\ 0 & n_y^{(k)} \\ n_y^{(k)} & n_x^{(k)} \end{bmatrix} \tag{12}$$

In the NS-FEM-T3, the trial function $\mathbf{u}^h(\mathbf{x})$ is the same as in Equation (2) of the FEM and therefore the force vector $\mathbf{f}$ in the NS-FEM-T3 is calculated in the same way as in the FEM.

Substituting Equation (2) into (11), the smoothed strain on the cell $\Omega^{(k)}$ associated with node k can be written in the following matrix form of nodal displacements:

$$\tilde{\boldsymbol{\varepsilon}}_k = \sum_{I \in N^{(k)}} \tilde{\mathbf{B}}_I(\mathbf{x}_k)\mathbf{d}_I \tag{13}$$

where $N^{(k)}$ is the set containing nodes that are directly connected to node k and $\tilde{\mathbf{B}}_I(\mathbf{x}_k)$ is termed as the *smoothed strain gradient matrix* on the cell $\Omega^{(k)}$

$$\tilde{\mathbf{B}}_I(\mathbf{x}_k) = \begin{bmatrix} \tilde{b}_{Ix}(\mathbf{x}_k) & 0 \\ 0 & \tilde{b}_{Iy}(\mathbf{x}_k) \\ \tilde{b}_{Iy}(\mathbf{x}_k) & \tilde{b}_{Ix}(\mathbf{x}_k) \end{bmatrix} \tag{14}$$

and it is calculated numerically using

$$\tilde{b}_{Ih}(\mathbf{x}_k) = \frac{1}{A^{(k)}} \int_{\Gamma^{(k)}} N_I(\mathbf{x}) n_h^{(k)}(\mathbf{x})\,\mathrm{d}\Gamma \quad (h = x, y) \tag{15}$$

Using the linear shape function of triangles as in Equation (2) of the FEM-T3, the displacement field in the NS-FEM-T3 is linear compatible along the boundary $\Gamma^{(k)}$. Hence, one Gaussian point

DOI: 10.1002/cnm

is sufficient for line integration along each segment of boundary $\Gamma_i^{(k)} \in \Gamma^{(k)}$, the above equation can be further simplified to its algebraic form

$$\tilde{b}_{Ih}(\mathbf{x}_k) = \frac{1}{A^{(k)}} \sum_{i=1}^{M} N_I(\mathbf{x}_i^{\mathrm{GP}}) n_{ih}^{(k)} l_i^{(k)} \quad (h = x, y) \tag{16}$$

where M is the total number of the boundary segments of $\Gamma_i^{(k)}$, $\mathbf{x}_i^{\mathrm{GP}}$ is the midpoint (Gaussian point) of the boundary segment of $\Gamma_i^{(k)}$, whose length and outward unit normal are denoted as $l_i^{(k)}$ and $n_{ih}^{(k)}$, respectively.

The stiffness matrix $\tilde{\mathbf{K}}$ of the system is then assembled by a similar process as in the FEM

$$\tilde{\mathbf{K}}_{IJ} = \sum_{k=1}^{N_n} \tilde{\mathbf{K}}_{IJ}^{(k)} \tag{17}$$

where $\tilde{\mathbf{K}}_{IJ}^{(k)}$ is the stiffness matrix associated with node k and is calculated by

$$\tilde{\mathbf{K}}_{IJ}^{(k)} = \int_{\Omega^k} \tilde{\mathbf{B}}_I^{\mathrm{T}} \mathbf{D} \tilde{\mathbf{B}}_J \, \mathrm{d}\Omega = \tilde{\mathbf{B}}_I^{\mathrm{T}} \mathbf{D} \tilde{\mathbf{B}}_J A^{(k)} \tag{18}$$

Equation (16) implies that in the NS-FEM-T3, field gradients are computed directly only using the values of shape functions themselves at some particular points along segments of boundary $\Gamma_i^{(k)}$ and no derivative of shape function is needed.

When the linear shape functions for triangular elements are used, displacement field along the boundaries $\Gamma^{(k)}$ of the domain $\Omega^{(k)}$ is linear compatible. The values of the shape functions of these Gauss points, e.g. point #a on segment A–B shown in Figure 5, are evaluated averagely using two related points at two segment's ends: points #A and #B. To facilitate for the computation, the values of the shape functions at ending points of segments are performed explicitly as follows: (1) for the point at the mid-side of the element, e.g. point #A on the side 1–2, the values of the shape functions are evaluated averagely using two related field nodes: nodes #1 and #2; (2) for

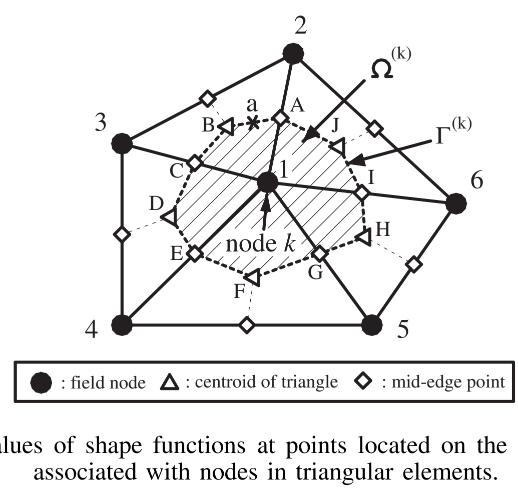

Figure 5. Evaluation of values of shape functions at points located on the boundary of smoothing cell associated with nodes in triangular elements.

DOI: 10.1002/cnm

the point at the centroid of the element, e.g. point #B of the element 1–2–3, values of the shape function are evaluated as $[\frac{1}{3}\ \frac{1}{3}\ \frac{1}{3}]$, which is the average values using three related field nodes: node #1, #2 and #3.

It should be mentioned that the purpose of introducing the centroid points is to facilitate the evaluation of the shape function values at the Gauss points along the segments of the smoothing domain. No extra degrees of freedom (DOF) are associated with these points. In other words, these points carry no additional field variables. This means that the nodal unknowns in the NS-FEM-T3 are the same as those in the FEM-T3 of the same mesh.

2.3. *A brief of properties of the NS-FEM*

The following properties of the NS-FEM were presented by Liu *et al.* [24]. In this paper, we only remind the main points.

Property 1: The NS-FEM can be derived straightforwardly from the modified Hellinger–Reissner variational principle, with the smoothed strain vector $\tilde{\boldsymbol{\varepsilon}}_k$ and displacements $\mathbf{u}^h(\mathbf{x})$ as independent field variables, to give the stiffness matrix associated with nodes $\tilde{\mathbf{K}}_{IJ}^{(k)}$ in the form of Equations (17) and (18). The method is therefore variationally consistent.

Property 2: The strain energy $E(\mathbf{d})$ obtained from the NS-FEM solution has the following relationship with the exact strain energy:

$$E(\mathbf{d}) \geqslant E_{\text{exact}}(\mathbf{d}_0) \tag{19}$$

where $\mathbf{d}$ is the numerical solution of the NS-FEM, and $\mathbf{d}_0$ is the exact displacement sampled using the exact displacement field $\mathbf{u}_0$.

Property 3: The NS-FEM possesses only 'legal' zero energy modes that represent the rigid motions, and there exists no spurious zero energy mode.

Property 4: The NS-FEM is immune from the volumetric locking.

3. ADAPTIVE PROCEDURE

In an adaptive procedure, a good error indicator and an appropriate refinement strategy are two important issues needed to be considered. In this present work, an error indicator based on the recovery strain is proposed and shown to be asymptotically exact by an effectivity index and numerical experiments. Then, a simple refinement strategy using the newest node bisection is briefly presented.

3.1. *Error indicator based on recovery strain*

For each element Ω_e, we will use

$$\eta_e = \|\nabla\mathbf{u} - \tilde{\boldsymbol{\varepsilon}}^h\|_{L_2(\Omega_e)} \tag{20}$$

as the error indicator, where $\nabla\mathbf{u}$ is the exact strain and $\tilde{\boldsymbol{\varepsilon}}^h$ is the numerical strain of the element in the NS-FEM-T3 as shown in Figure 6. However, to determine the error indicator (20) without knowing the exact solution, a higher-order recovery strain $\mathbf{Gu}$ of $\nabla\mathbf{u}$ need to be constructed using only $\tilde{\boldsymbol{\varepsilon}}^h$. This means that the approximation $\mathbf{Gu}$ has to be more accurate than $\tilde{\boldsymbol{\varepsilon}}^h$ in the meaning

$$\|\nabla\mathbf{u} - \mathbf{Gu}\|_{L_2(\Omega_e)} \leqslant C_1 h^{\alpha} \|\nabla\mathbf{u} - \tilde{\boldsymbol{\varepsilon}}^h\|_{L_2(\Omega_e)}, \quad \alpha > 0 \tag{21}$$

DOI: 10.1002/cnm

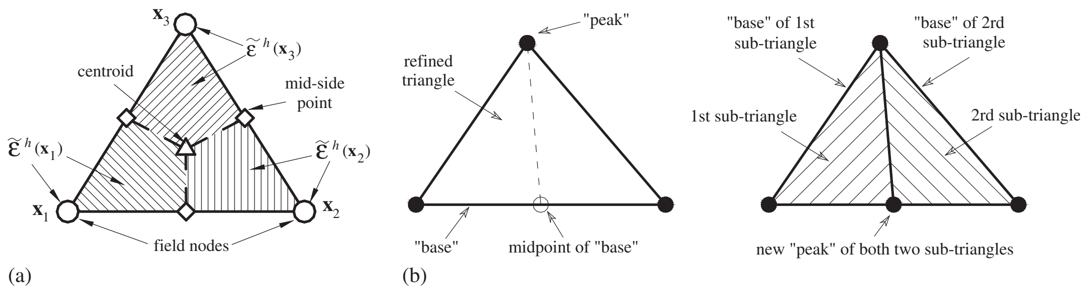

Figure 6. (a) Stresses at three field nodes and three quadrilateral sub-domains of the element in the NS-FEM and (b) division of the refined triangle into two sub-triangles using the newest node bisection.

Equation (21) can be verified if the following effectivity index $\theta = \|\tilde{\boldsymbol{\varepsilon}}^h - \mathbf{Gu}\|_{L_2(\Omega_e)} / \|\tilde{\boldsymbol{\varepsilon}}^h - \nabla\mathbf{u}\|_{L_2(\Omega_e)}$, which is a measure of the error estimate compared with the exact error, converges to unity when h approaches zero [7, 8]. The verification process starts from

$$\|\tilde{\boldsymbol{\varepsilon}}^h - \mathbf{Gu}\|_{L_2(\Omega_e)} = \|(\tilde{\boldsymbol{\varepsilon}}^h - \nabla\mathbf{u}) - (\mathbf{Gu} - \nabla\mathbf{u})\|_{L_2(\Omega_e)} \tag{22}$$

Using the triangle inequality, we have

$$\|\tilde{\boldsymbol{\varepsilon}}^h - \nabla\mathbf{u}\|_{L_2(\Omega_e)} - \|\mathbf{Gu} - \nabla\mathbf{u}\|_{L_2(\Omega_e)} \leqslant \|\tilde{\boldsymbol{\varepsilon}}^h - \mathbf{Gu}\|_{L_2(\Omega_e)} \leqslant \|\tilde{\boldsymbol{\varepsilon}}^h - \nabla\mathbf{u}\|_{L_2(\Omega_e)} + \|\mathbf{Gu} - \nabla\mathbf{u}\|_{L_2(\Omega_e)} \tag{23}$$

Then by dividing each term by $\|\tilde{\boldsymbol{\varepsilon}}^h - \nabla\mathbf{u}\|_{L_2(\Omega_e)}$, we obtain

$$1 - \frac{\|\mathbf{Gu} - \nabla\mathbf{u}\|_{L_2(\Omega_e)}}{\|\tilde{\boldsymbol{\varepsilon}}^h - \nabla\mathbf{u}\|_{L_2(\Omega_e)}} \leqslant \theta \leqslant 1 + \frac{\|\mathbf{Gu} - \nabla\mathbf{u}\|_{L_2(\Omega_e)}}{\|\tilde{\boldsymbol{\varepsilon}}^h - \nabla\mathbf{u}\|_{L_2(\Omega_e)}} \tag{24}$$

As proved by Zienkiewicz and Zhu in [7, 8], Equation (21) is verified if the effectivity index θ approach 1 as h approaches zero. In that case, the recovery solution $\mathbf{Gu}$ converges at a higher rate than the numerical solution $\tilde{\boldsymbol{\varepsilon}}^h$, and we shall have asymptotically exact estimation: the error $\|\mathbf{Gu} - \tilde{\boldsymbol{\varepsilon}}^h\|_{L_2(\Omega_e)}$ will approach to $\|\nabla\mathbf{u} - \tilde{\boldsymbol{\varepsilon}}^h\|_{L_2(\Omega_e)}$.

In this paper, by using smoothed strain $\tilde{\boldsymbol{\varepsilon}}^h(\mathbf{x}_j)$ defined in Equation (8) as the 'nodal' strain at the node $\mathbf{x}_j$ as shown in Figure 6, we construct a first-order recovery strain $\mathbf{Gu}$ for each element by the following interpolation [46, 47]:

$$\mathbf{Gu} = \sum_{j=1}^{3} \mathbf{N}_j(\mathbf{x}) \tilde{\boldsymbol{\varepsilon}}^h(\mathbf{x}_j) \tag{25}$$

where $\mathbf{N}_j(\mathbf{x})$ are the same linear shape functions of triangular elements used to define $\mathbf{u}^h$ in Equation (2).

The numerical examples in Section 4 will illustrate clearly the effectiveness and reliability of the error indicator (20) in which the exact strain $\nabla\mathbf{u}$ is replaced by the first-order recovery strain $\mathbf{Gu}$ in Equation (25). In numerical performance of the error indicator (20), the usual Gauss integration with proper mapping procedure is performed for each of three quadrilateral sub-domains as shown in Figure 6, and the summation over these three quadrilateral sub-domains is then performed for the element.

DOI: 10.1002/cnm

3.2. Refinement strategy

Let us first define the marking scheme used with the error indicator. Let

$$\eta^2 = \sum_{e=1}^{N_e} \eta_e^2 \tag{26}$$

be an global error indicator with all the elemental contributions η_e associated with a triangle Ω_e. We will use the bulk marking process proposed by Dorfler [48] in which the marking set M that contains the marked elements to be refined at a single step. Elements in set M should satisfy the following criteria

$$\sum_{\Omega_e \in M} \eta_e^2 \geqslant \theta \eta^2 \quad \text{for some } \theta \in (0, 1) \tag{27}$$

A smaller θ will result in a larger set M and hence a more refinement of triangles at one step, and a larger θ will result in a smaller set M and thus a more optimal mesh but more refinement steps. Usually $\theta = 0.2 \div 0.5$ is chosen.

Now, a refinement strategy using the newest node bisection is briefly presented [49, 50]. First, a process of labeling is performed. From a triangulation set Ψ of the problem domain Ω, for each triangle $\Omega_e \in \Psi$, one node of Ω_e is labeled as peak or newest node. The opposite edge of the peak is called base or refinement edge as shown in Figure 6(b). Then the division of the refined triangle into two sub-triangles using the newest node bisection is conducted as follows:

(i) a refined triangle is bisected to two new sub-triangles by connecting the peak to the midpoint of the base as shown in Figure 6(b);
(ii) the new node created at a midpoint of a base is assigned to be the peak of both sub-triangles as shown in Figure 6(b).

Once an initial triangulation is labeled, the proper triangulations inherit the label by the rule (ii) such that the bisection process can continue. Refinement scheme using the newest node bisection will not lead to a degeneracy and is easy to implement since the conforming is ensured in the marking step.

4. NUMERICAL RESULTS

In order to simplify the notation, from this section until the end, we will shorten NS-FEM-T3 by NS-FEM, and FEM-T3 by FEM.

To study the effectiveness of the present adaptive procedure, uniformly refined models of NS-FEM are also considered. In addition, to emphasize the upper bound property of strain energy of the NS-FEM, the results of the present method will be compared with those of the standard linear FEM using both adaptive procedure and uniformly refined models. For the adaptive procedure using the FEM, the same error indicator and refinement algorithm used in the adaptive procedure of NS-FEM are used. However in the FEM, to obtain the first-order recovery strain $\mathbf{Gu}$ as shown in Equation (25), we will use the simplest Zienkiewicz–Zhu recovery [6], in which the strains at a node are the averaged strains at the centroids of the patch of elements surrounding the node. Therefore, the comparison is done in a fair base.

DOI: 10.1002/cnm

In some cases, in order to evaluate the accuracy and convergence rate of the present scheme, the following energy norm is used:

$$\|\boldsymbol{\varepsilon}-\boldsymbol{\varepsilon}^L\|_{L_2}=\left(\frac{1}{2}\int_{\Omega}(\boldsymbol{\varepsilon}-\boldsymbol{\varepsilon}^L)^{\mathrm{T}}\mathbf{D}(\boldsymbol{\varepsilon}-\boldsymbol{\varepsilon}^L)\,\mathrm{d}\Omega\right)^{1/2}=\left(\frac{1}{2}\sum_{e=1}^{N_e}\int_{\Omega_e}(\boldsymbol{\varepsilon}-\boldsymbol{\varepsilon}^L)^{\mathrm{T}}\mathbf{D}(\boldsymbol{\varepsilon}-\boldsymbol{\varepsilon}^L)\,\mathrm{d}\Omega\right)^{1/2} \tag{28}$$

where $\boldsymbol{\varepsilon}$ is the analytical strain and $\boldsymbol{\varepsilon}^L$ is one of two strains: the numerical strain $\boldsymbol{\varepsilon}^h$ or first-order recovery strain $\boldsymbol{\varepsilon}^{\mathrm{Re}}\equiv\mathbf{Gu}$.

In order to evaluate the integral in Equation (28) for each triangular element Ω_e, when $\boldsymbol{\varepsilon}^L$ is the numerical strain of NS-FEM, the mapping procedure using Gauss integration on quadrilateral sub-domains of triangles mentioned in the end of Section 3.1 is used, and the summation on three quadrilateral sub-domains is done. However, in each quadrilateral sub-domain, a suitable number of Gauss points depending on the order of the analytical solution will be used. Otherwise, when $\boldsymbol{\varepsilon}^L$ is the numerical strain of FEM or the recovery strains $\boldsymbol{\varepsilon}^{\mathrm{Re}}\equiv\mathbf{Gu}$ of both NS-FEM and FEM, the mapping procedure using Gauss integration is performed on triangular elements. In each triangle, a suitable number of Gauss points depending on the order of the analytical solution will be used.

In addition, in adaptive analysis, in order to estimate the energy error norms by Equation (28) without having the analytical strain, the recovery strain $\boldsymbol{\varepsilon}^{\mathrm{Re}}\equiv\mathbf{Gu}$ will be used to replace the analytical strain. Note that the convergence rates of the energy error norms are calculated based on the average length of sides of triangular elements.

4.1. *Infinite plate with a circular hole*

Figure 7 represents a plate with a central circular hole of radius $a=1\,\mathrm{m}$, subjected to a unidirectional tensile load of $\sigma=1.0\,\mathrm{N/m}$ at infinity in the x-direction. Owing to its symmetry, only the upper right quadrant of the plate is modeled. Plane strain condition is considered and $E=1.0\times10^3\,\mathrm{N/m^2}$, $\nu=0.3$. Symmetric conditions are imposed on the left and bottom edges, and the inner boundary of the hole is traction free. The exact solution for the stress is [51]

$$\begin{aligned}\sigma_{11}&=1-\frac{a^2}{r^2}\left[\frac{3}{2}\cos2\theta+\cos4\theta\right]+\frac{3a^4}{2r^4}\cos4\theta\\ \sigma_{22}&=-\frac{a^2}{r^2}\left[\frac{1}{2}\cos2\theta-\cos4\theta\right]-\frac{3a^4}{2r^4}\cos4\theta\end{aligned} \tag{29}$$

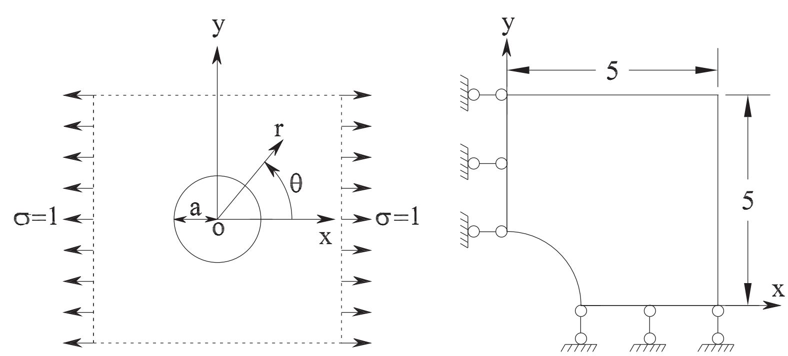

Figure 7. Infinite plate with a circular hole and its quarter model.

DOI: 10.1002/cnm

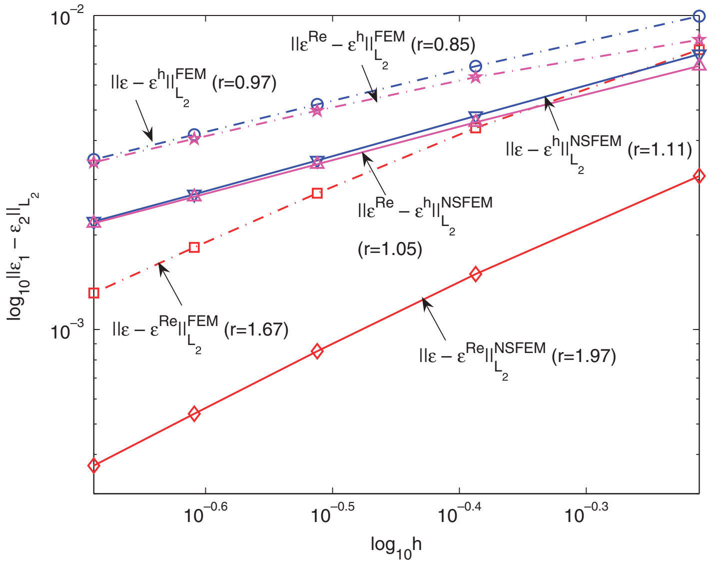

Figure 8. Energy error norms of the infinite plate with a circular hole ($\boldsymbol{\varepsilon}_1$ in the vertical axe represents for $\boldsymbol{\varepsilon}$ or $\boldsymbol{\varepsilon}^{\mathrm{Re}}$, and $\boldsymbol{\varepsilon}_2$ represents for $\boldsymbol{\varepsilon}^h$ or $\boldsymbol{\varepsilon}^{\mathrm{Re}}$).

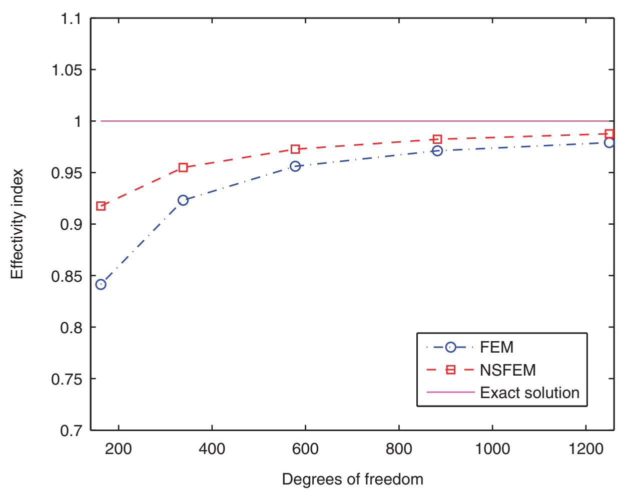

Figure 9. Effectivity index of the infinite plate with a circular hole.

$$\tau_{12} = -\frac{a^2}{r^2}\left[\frac{1}{2}\sin 2\theta + \sin 4\theta\right] + \frac{3a^4}{2r^4}\sin 4\theta$$

where (r, θ) are the polar coordinates and θ is measured counterclockwise from the positive x-axis. Traction boundary conditions are imposed on the right ($x = 5.0$) and top ($y = 5.0$) edges based on the exact solution Equation (29). The displacement components corresponding to the stresses are

DOI: 10.1002/cnm

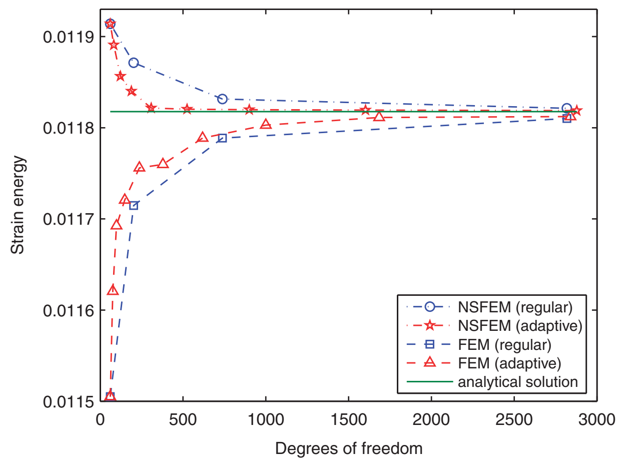

Figure 10. Convergence of strain energy in the infinite plate with a circular hole.

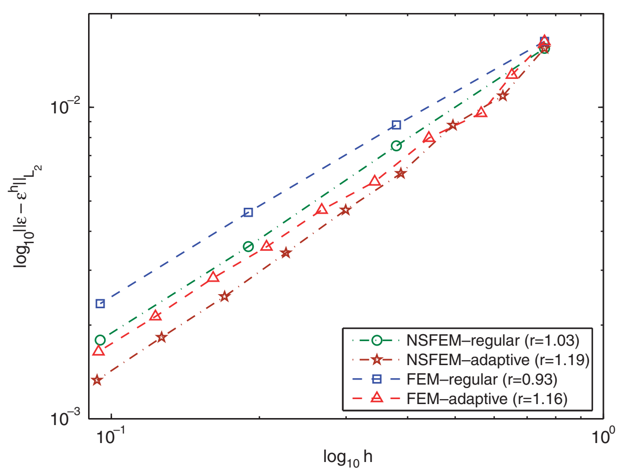

Figure 11. Comparison of energy error norms in the infinite plate with a circular hole.

$$\begin{aligned} u_1 &= \frac{a}{8\mu}\left[\frac{r}{a}(\kappa+1)\cos\theta+2\frac{a}{r}((1+\kappa)\cos\theta+\cos 3\theta)-2\frac{a^3}{r^3}\cos 3\theta\right] \\ u_2 &= \frac{a}{8\mu}\left[\frac{r}{a}(\kappa-1)\sin\theta+2\frac{a}{r}((1-\kappa)\sin\theta+\sin 3\theta)-2\frac{a^3}{r^3}\sin 3\theta\right] \end{aligned} \tag{30}$$

where $\mu = E/(2(1+\nu))$, κ is defined in terms of Poisson's ratio by $\kappa = 3-4\nu$ for plane strain cases.

First, one analysis about the accuracy and convergence rate of energy error norms, and effectivity index of the error indicators of NS-FEM and FEM are performed by using uniformly refined models. Three kinds of energy error norms are evaluated including the standard energy error norm $\|\boldsymbol{\varepsilon}-\boldsymbol{\varepsilon}^h\|_{L_2}$, recovery energy error norm $\|\boldsymbol{\varepsilon}-\boldsymbol{\varepsilon}^{\mathrm{Re}}\|_{L_2}$ and *a posteriori* energy error norm

DOI: 10.1002/cnm

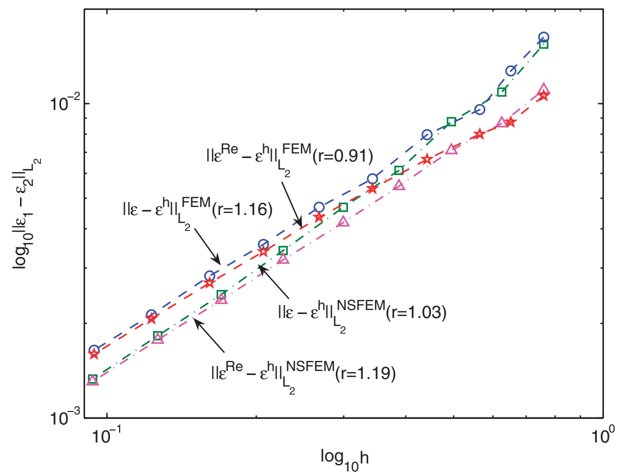

Figure 12. Comparison of energy error norms and error estimators (20) in the infinite plate with a circular hole ($\boldsymbol{\varepsilon}_1$ in the vertical axe represents for $\boldsymbol{\varepsilon}$ or $\boldsymbol{\varepsilon}^{\mathrm{Re}}$, and $\boldsymbol{\varepsilon}_2$ represents for $\boldsymbol{\varepsilon}^h$).

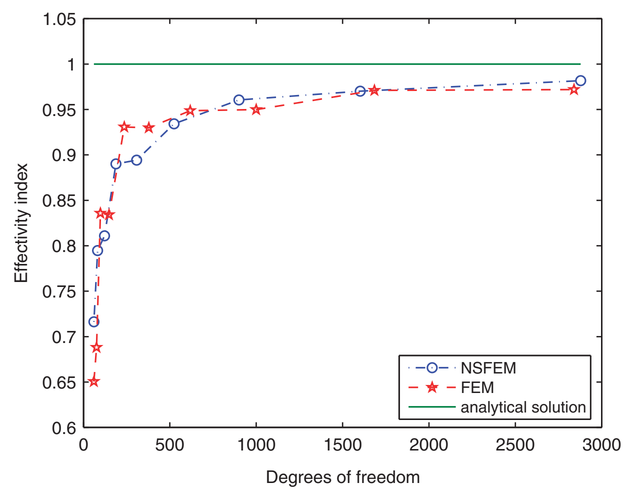

Figure 13. Effectivity index (adaptive scheme) of NS-FEM and FEM in the infinite plate with a circular hole.

$\|\boldsymbol{\varepsilon}^{\mathrm{Re}}-\boldsymbol{\varepsilon}^h\|_{L_2}$, where $\boldsymbol{\varepsilon}^h$ is the numerical strain of methods, $\boldsymbol{\varepsilon}^{\mathrm{Re}} \equiv \mathbf{Gu}$ is the first-order recovery strain and $\boldsymbol{\varepsilon}$ is the analytical strain.

Figures 8 and 9 show four following remarks: (1) in each method, the recovery energy error norm $\|\boldsymbol{\varepsilon}-\boldsymbol{\varepsilon}^{\mathrm{Re}}\|_{L_2}$ are much more accurate than standard and *posteriori* energy error norms; (2) for standard and *posteriori* energy error norms, the results of NS-FEM are more accurate than those of FEM, and the convergence rates of NS-FEM are also higher than those of FEM; (3) the recovery energy error norms $\|\boldsymbol{\varepsilon}-\boldsymbol{\varepsilon}^{\mathrm{Re}}\|_{L_2}$ of both NS-FEM and FEM are super-convergent but

DOI: 10.1002/cnm

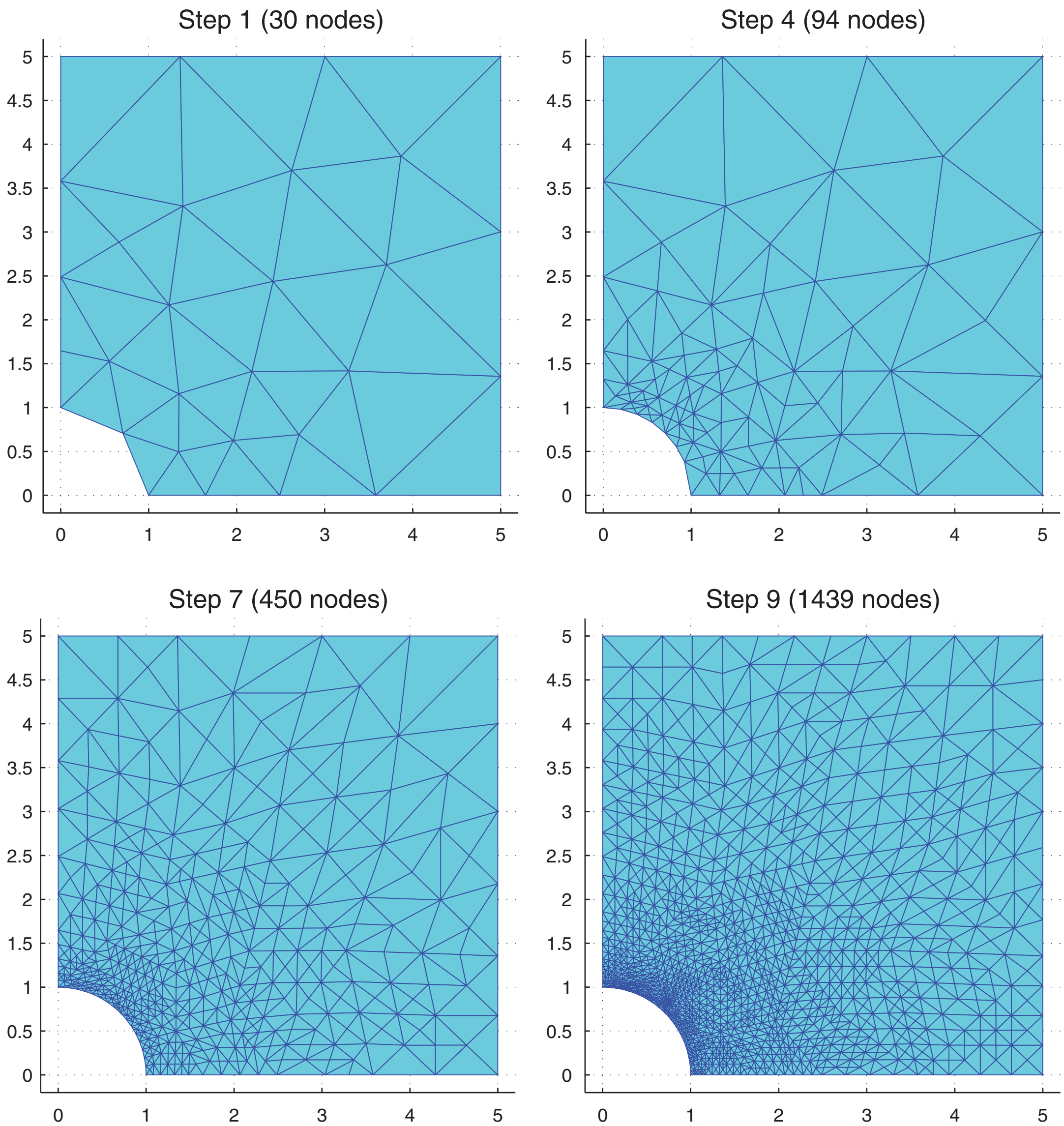

Figure 14. Sequence of adaptive refinement models for the quarter of plate using NS-FEM.

the convergence rate of NS-FEM ($r=1.97$) is much higher than that of FEM ($r=1.67$). The super-convergence of the recovery energy error norm $\|\boldsymbol{\varepsilon}-\boldsymbol{\varepsilon}^{\mathrm{Re}}\|_{L_2}$ of NS-FEM almost equal to that of CS-FEM (or SFEM) using 1 SC for each quadrilateral element [22, 23, 52]; (4) the effectivity indexes θ of the error indicators of both NS-FEM and FEM approach to unity when the mesh is refined, but the results of NS-FEM are closer to unity than those of FEM, especially for coarse meshes. The results of effectivity indexes θ of the error indicators in Figure 9 are also illustrated

DOI: 10.1002/cnm

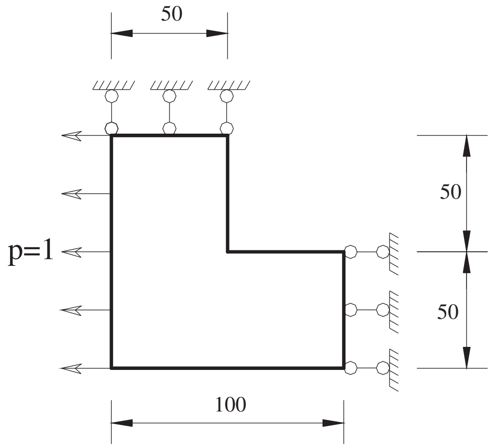

Figure 15. Model of L-shaped domain.

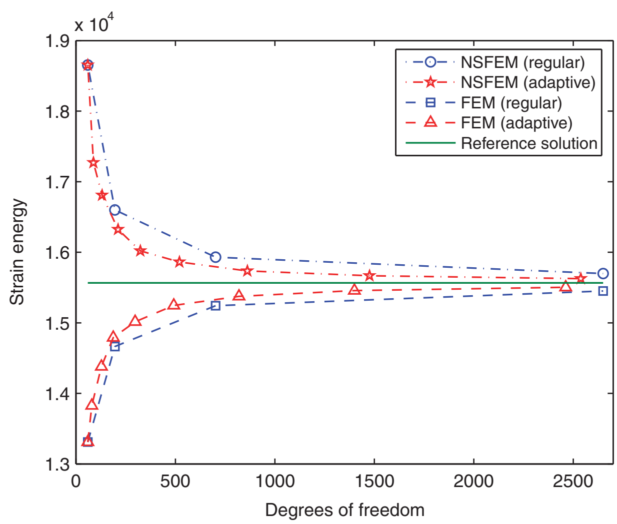

Figure 16. Strain energy in the L-shaped problem with applied tractions.

clearly in Figure 8, in which the standard energy error norms are very close to the *posteriori* energy error norms for both methods.

These results verify the asymptotically exact property of the error estimator $\|\mathbf{Gu}-\tilde{\boldsymbol{\varepsilon}}^h\|_{L_2}$ in Section 3, and also show that the error estimator $\|\mathbf{Gu}-\tilde{\boldsymbol{\varepsilon}}^h\|_{L_2}$ of NS-FEM is more reliable than that of FEM. In other words, the recovery strain field $\boldsymbol{\varepsilon}^{\mathrm{Re}} \equiv \mathbf{Gu}$ of the NS-FEM is a very good representation of the exact strain field, and using it to obtain energy error estimates is feasible and more reliable than using the recovery strain field of the FEM used in this paper.

DOI: 10.1002/cnm

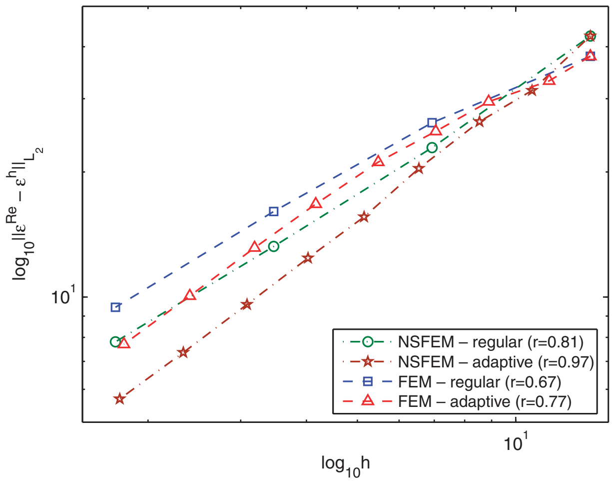

Figure 17. Comparison of energy error norms using the error indicator (20) in L-shaped problem with applied tractions.

Now, we can conduct the adaptive analysis for the problem. The results of the strain energy and standard energy error norms of NS-FEM and FEM with both uniform and adaptive models are shown in Figure 10 and Figure 11. First, the results show that the adaptive models for both NS-FEM and FEM have much higher convergence rates compared to the uniformly refined models. This demonstrates the effectiveness of the presented adaptive procedure. Second, compared with the linear FEM, the NS-FEM achieves a better accuracy and higher convergence rate for both uniform and adaptive models. Third, the upper bound property in the strain energy of the NS-FEM is always verified during the adaptive procedure.

Figure 12 compares the standard energy error norms and error estimators (20) (the posteriori energy error norms) of NS-FEM and FEM. The results again show that the standard energy error norms are very close to the error estimators (20) for both methods, but the results of NS-FEM are better and have higher convergence rate than those of FEM. Figure 13 again verifies the asymptotically exact property of the error estimator (20) in which the effectivity indexes of adaptive schemes for both methods converge to unity when the mesh is refined.

Figure 14 shows the sequence of the models produced during the adaptive refinement steps using NS-FEM. The results show that the refinement is most active in the regions with significant stress concentration, as expected.

4.2. L-shaped domain with applied tractions

Consider an L-shaped domain subjected to a unit tension. The dimensions and boundary conditions are shown in Figure 15. The thickness of the solid is $t = 1\,\text{m}$, and a plane stress problem is considered. The material parameters of the structure are $E = 1.0\,\text{N/m}^2$, $\nu = 0.3$. In this example, a stress singularity occurs at the re-entrant corner.

The exact strain energy in this problem is not available. However, it can be estimated through the procedure of Richardson's extrapolation [53] from the solutions of the displacement models and equilibrium models [54]. The estimated strain energy is average of these two extrapo-

DOI: 10.1002/cnm

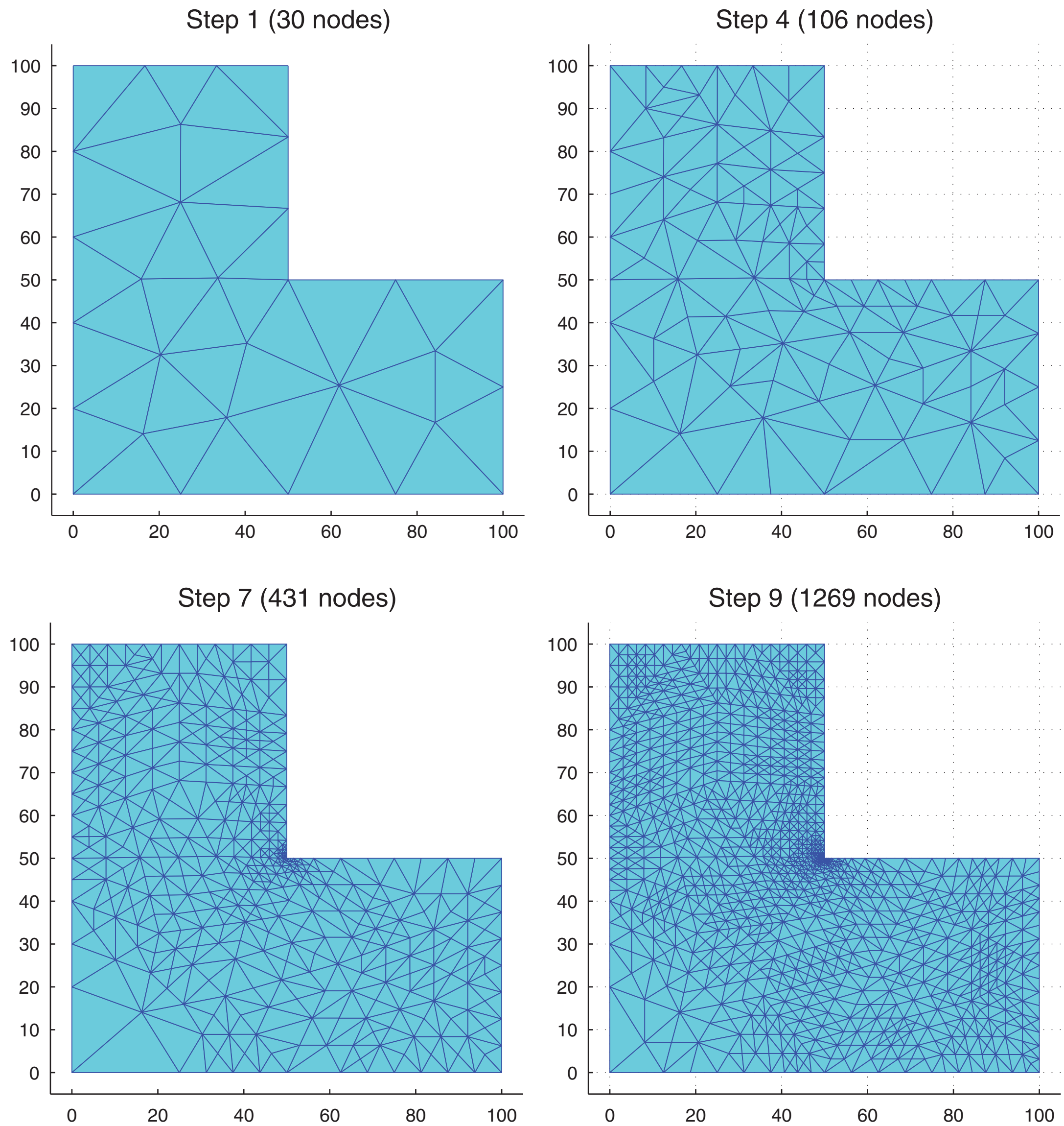

Figure 18. Sequence of adaptive refinement models for the L-shaped domain using NS-FEM.

lated strain energies. As given in Reference [55], the reference strain energy is approximately 15 566.460.

The results of posteriori energy error norms of NS-FEM and FEM using both uniform and adaptive models versus degrees of freedom (DOF) are shown in Figure 17. Again, the results show that the adaptive models for both NS-FEM and FEM give higher convergence rate compared to the uniformly refined models. The results of NS-FEM are better and give higher convergence rate

DOI: 10.1002/cnm

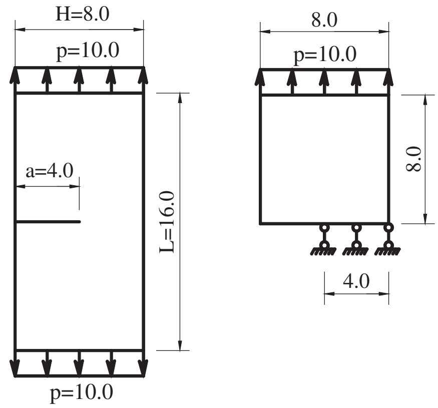

Figure 19. Crack problem and half of the domain modeled.

than those of FEM. For this problem, we have not the analytical solution. Therefore, we cannot show the super-convergence of the recovery energy error norm between the analytical and recovery strains. However, basing on the convergence rate of the posteriori energy error norm of NS-FEM ($r = 0.97$) which is almost 1, we can see that the recovery strain is a reliable representation of the analytical strain and can produce efficiently an optimal convergence in energy norm for this singular problem.

Figure 16 verifies the upper bound property in the strain energy of the NS-FEM during the adaptive procedure. Figure 18 shows the some steps of adaptive refinement models using NS-FEM. The results show clearly that the refinement is focusing on the re-entrant corner where the concentration of stress occurs.

4.3. Crack problem in linear elasticity

Consider a crack problem in linear elasticity as shown in Figure 19. Data of the structure are $E = 1.0\,\mathrm{N/m^2}$, $\nu = 0.3$, $t = 1\,\mathrm{m}$. Owing to the symmetry about the x-axis, only half of domain is modeled. By incorporating the dual analysis [56] and the procedure of Richardson's extrapolation with very fine meshes, Beckers [55] proposed a good approximation of the exact strain energy to be 8085.7610.

This crack problem has a high singularity at the crack tip. As a result, the convergence rate of the posteriori energy error norms between the recovery and numerical strains using the uniformly refined models is low ($r = 0.35$ for FEM and $r = 0.55$ for NS-FEM). The adaptive schemes are therefore very necessary to be applied to improve the convergence rate. The results in Figure 21 show that the posteriori energy error norms of adaptive models for both NS-FEM and FEM have higher convergence rate compared to the uniformly refined models, but the results of NS-FEM are better and have higher convergence rate than those of FEM. Without having the analytical solution, we cannot show the super-convergence of the recovery energy error norm between the analytical and recovery strains. However, based on the convergence rate of the posteriori energy error norm of NS-FEM ($r = 0.97$) which is almost 1, we can see that the recovery strain is a reliable representation of the analytical strain and can produce efficiently an optimal convergence

DOI: 10.1002/cnm

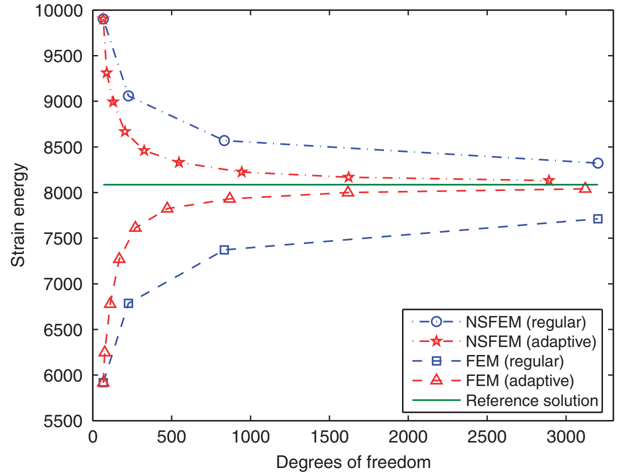

Figure 20. Convergence of strain energy of the crack problem.

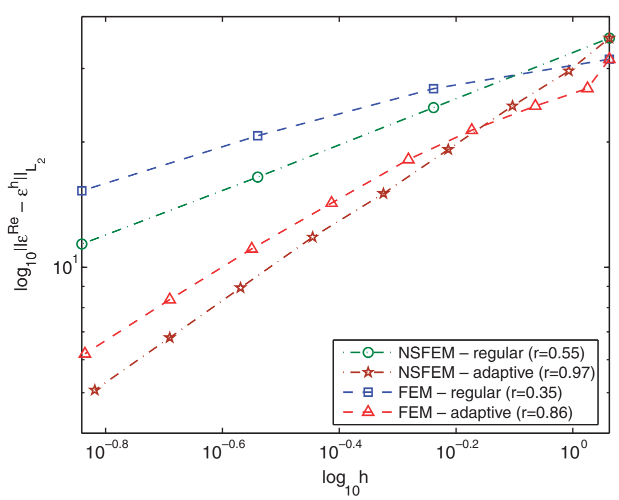

Figure 21. Comparison of strain energy error norms of crack problem.

in energy norm for this strongly singular case. Note that, for this problem, adaptive schemes using enrichment techniques as in the XFEM [57, 58] also give very good results.

Figure 20 verifies the upper bound property in the strain energy of the NS-FEM during the adaptive procedure. Figure 22 shows the some steps of adaptive refinement models using NS-FEM. The results show clearly that the refinement is focusing on the crack tip where the singularity appears.

DOI: 10.1002/cnm

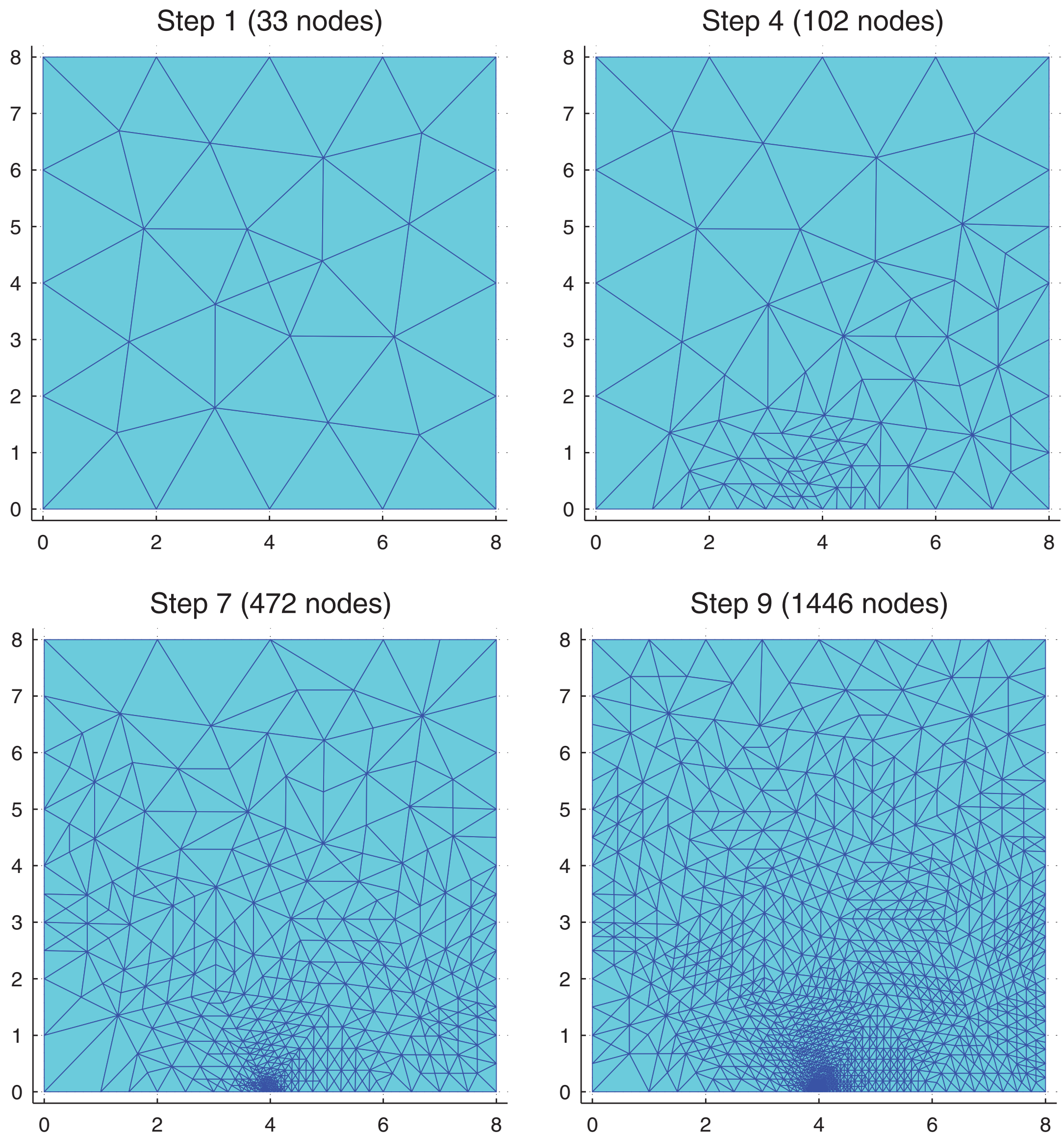

Figure 22. Sequence of adaptive refinement models for the crack problem using NS-FEM.

5. CONCLUSION

In this work, an adaptive procedure for NS-FEM using triangular elements is proposed. An error indicator based on the recovery strain is proposed and shown to be asymptotically exact by numerical experiments through an effectivity index, and a simple refinement strategy using the newest node bisection is briefly presented. The numerical results of some benchmark problems

DOI: 10.1002/cnm

show that the present adaptive procedure can accurately catch the appearance of the steep gradient of stresses and the occurrence of refinement is concentrated properly. The upper bound property in the strain energy of the NS-FEM is always verified during the adaptive procedure, and the effectivity index of the proposed error indicator approaches unity faster than that of FEM. Compared with uniformly refined models, adaptive models achieve very high reliability and effectiveness.

REFERENCES

1. Babuska I, Rheinboldt C. A-posteriori error estimates for the finite element method. *International Journal for Numerical Methods in Engineering* 1978; **12**:1597–1615.
2. Babuska I, Rheinboldt C. Adaptive approaches and reliability estimates in finite element analysis, error estimates for the finite element method. *Computer Methods in Applied Mechanics and Engineering* 1979; **17–18**:519–540.
3. Bank RA, Weiser A. Some a posteriori error estimators for elliptic partial differential equations. *Mathematics of Computation* 1985; **44**:283–301.
4. Ainsworth M, Oden JT. A procedure for a posteriori error estimation for h-p finite element methods. *Computer Methods in Applied Mechanics and Engineering* 1992; **101**:73–96.
5. Ainsworth M, Oden JT. A unified approach to a posteriori error estimation using element residual methods. *Numerische Mathematik* 1993; **65**:23–50.
6. Zienkiewicz OC, Zhu JZ. A simple error estimator and adaptive procedure for practical engineering analysis. *International Journal for Numerical Methods in Engineering* 1987; **24**:337–357.
7. Zienkiewicz OC, Zhu JZ. The superconvergence patch recovery and a posteriori error estimates. Part 1: the recovery techniques. *International Journal for Numerical Methods in Engineering* 1992; **33**:1331–1364.
8. Zienkiewicz OC, Zhu JZ. The superconvergence patch recovery and a posteriori error estimates. Part 2: error estimates and adaptivity. *International Journal for Numerical Methods in Engineering* 1992; **33**:1365–1382.
9. Ladevèze P, Leguillon D. Error estimate procedure in the finite element method and applications. *SIAM Journal on Numerical Analysis* 1983; **20**:483–509.
10. Ladevèze P, Rougeot PH. New advances on a posteriori error on constitutive relation in f.e. analysis. *Computer Methods in Applied Mechanics and Engineering* 1997; **150**:239–249.
11. Florentin E, Gallimard L, Ladevèze P, Pelle JP. Local error estimator for stresses in 3D structural analysis. *Computers and Structures* 2003; **81**:1751–1757.
12. Zienkiewicz OC, Taylor RL. *The Finite Element Method* (5th edn). Butterworth Heinemann: Oxford, 2000.
13. Huerta A, Rodridguez-ferran A, Didez P, Sarrate J. Adaptive finite element strategies based on error assessment. *International Journal for Numerical Methods in Engineering* 1999; **46**:1803–1818.
14. Duflot M, Bordas S. A posteriori error estimation for extended finite elements by an extended global recovery. *International Journal for Numerical Methods in Engineering* 2008; **76**:1123–1138.
15. Xiao QZ, Karihaloo BL. Improving the accuracy of XFEM crack tip fields using higher order quadrature and statically admissible stress recovery. *International Journal for Numerical Methods in Engineering* 2006; **66**:1378–1410.
16. Bordas S, Duflot M, Le P. A simple error estimator for extended finite elements. *Communications in Numerical Methods in Engineering* 2008; **24**:961–971.
17. Bordas S, Duflot M. Derivative recovery and a posteriori error estimate for extended finite elements. *Computer Methods in Applied Mechanics and Engineering* 2007; **196**:3381–3399.
18. Chen JS, Wu CT, Yoon S, You Y. A stabilized conforming nodal integration for Galerkin meshfree method. *International Journal for Numerical Methods in Engineering* 2000; **50**:435–466.
19. Yoo JW, Moran B, Chen JS. Stabilized conforming nodal integration in the natural-element method. *International Journal for Numerical Methods in Engineering* 2004; **60**:861–890.
20. Liu GR, Zhang GY, Dai KY, Wang YY, Zhong ZH, Li GY, Han X. A linearly conforming point interpolation method (LC-PIM) for 2D solid mechanics problems. *International Journal of Computational Methods* 2005; **2**(4):645–665.
21. Liu GR, Li Y, Dai KY, Luan MT, Xue W. A linearly conforming radial point interpolation method for solid mechanics problems. *International Journal of Computational Methods* 2006; **3**(4):401–428.
22. Liu GR, Dai KY, Nguyen TT. A smoothed finite element method for mechanics problems. *Computational Mechanics* 2007; **39**:859–877.

DOI: 10.1002/cnm

23. Liu GR, Nguyen TT, Dai KY, Lam KY. Theoretical aspects of the smoothed finite element method (SFEM). *International Journal for Numerical Methods in Engineering* 2007; **71**:902–930.
24. Liu GR, Nguyen-Thoi T, Nguyen-Xuan H, Lam KY. A node-based smoothed finite element method for solid problems (NS-FEM). *Computers and Structures* 2009; **87**:14–26.
25. Liu GR, Nguyen-Thoi T, Nguyen-Xuan H, Dai KY, Lam KY. On the essence and the evaluation of the shape functions for the smoothed finite element method (SFEM) (Letter to Editor). *International Journal for Numerical Methods in Engineering* 2009; **77**:1863–1869.
26. Dai KY, Liu GR, Nguyen TT. An *n*-sided polygonal smoothed finite element method (nSFEM) for solid mechanics. *Finite Elements in Analysis and Design* 2007; **43**:847–860.
27. Dai KY, Liu GR. Free and forced analysis using the smoothed finite element method (SFEM). *Journal of Sound and Vibration* 2007; **301**:803–820.
28. Nguyen-Thoi T, Liu GR, Dai KY, Lam KY. Selective smoothed finite element method. *Tsinghua Science and Technology* 2007; **12**(5):497–508.
29. Nguyen-Xuan H, Bordas S, Nguyen-Dang H. Addressing volumetric locking and instabilities by selective integration in smoothed finite elements. *Communications in Numerical Methods and Engineering* 2008; **25**:19–34.
30. Nguyen-Xuan H, Rabczuk T, Bordas S, Debongnie JF. A smoothed finite element method for plate analysis. *Computer Methods in Applied Mechanics and Engineering* 2008; **197**:1184–1203.
31. Nguyen-Thanh N, Rabczuk T, Nguyen-Xuan H, Bordas S. A smoothed finite element method for shell analysis. *Computer Methods in Applied Mechanics and Engineering* 2008; **198**:165–177.
32. Nguyen-Xuan H, Nguyen-Thoi T. A stabilized smoothed finite element method for free vibration analysis of Mindlin-Reissner plates. *Communications in Numerical Methods in Engineering* 2009; DOI: 10.1002/cnm.1137.
33. Cui XY, Liu GR, Li GY, Zhao X, Nguyen-Thoi T, Sun GY. A smoothed finite element method (SFEM) for linear and geometrically nonlinear analysis of plates and shells. *CMES-Computer Modeling in Engineering and Sciences* 2008; **28**(2):109–125.
34. Nguyen-Van H, Mai-Duy N, Tran-Cong T. A smoothed four-node piezoelectric element for analysis of two-dimensional smart structures. *CMES—Computer Modeling in Engineering and Sciences* 2008; **23**(3):209–222.
35. Moes N, Dolbow J, Belytschko T. A finite element method for crack growth without remeshing. *International Journal for Numerical Methods in Engineering* 1999; **46**(1):131–150.
36. Bordas S, Rabczuk T, Nguyen-Xuan H, Nguyen Vinh P, Natarajan S, Bog T, Do Minh Q, Nguyen Vinh H. Strain smoothing in FEM and XFEM. *Computers and Structures* 2008. DOI: 10.1016/j.compstruc.2008.07.006.
37. Dohrmann CR, Heinstein MW, Jung J, Key SW, Witkowski WR. Node-based uniform strain elements for three-node triangular and four-node tetrahedral meshes. *International Journal for Numerical Methods in Engineering* 2000; **47**:1549–1568.
38. Liu GR, Zhang GY. Upper bound solution to elasticity problems: a unique property of the linearly conforming point interpolation method (LC-PIM). *International Journal for Numerical Methods in Engineering* 2008; **74**:1128–1161.
39. Liu GR, Nguyen-Thoi T, Lam KY. A novel alpha finite element method (αFEM) for exact solution to mechanics problems using triangular and tetrahedral elements. *Computer Methods in Applied Mechanics and Engineering* 2008; **197**:3883–3897.
40. Liu GR, Nguyen-Thoi T, Lam KY. An edge-based smoothed finite element method (ES-FEM) for static, free and forced vibration analyses of solids. *Journal of Sound and Vibration* 2009; **320**:1100–1130.
41. Nguyen-Thoi T, Liu GR, Nguyen-Xuan H. An *n*-sided polygonal edge-based smoothed finite element method (*n*ES-FEM) for solid mechanics. *Communications in Numerical Methods in Engineering* 2009; submitted.
42. Nguyen-Thoi T, Liu GR, Lam KY, Zhang GY. A face-based smoothed finite element method (FS-FEM) for 3D linear and nonlinear solid mechanics problems using 4-node tetrahedral elements. *International Journal for Numerical Methods in Engineering* 2009; **78**:324–353.
43. Nguyen-Xuan H, Liu GR, Nguyen-Thoi T, Nguyen-Tran C, An edge-based smoothed finite element method (ES-FEM) for analysis of two-dimensional piezoelectric structures. *Smart Materials and Structures* 2009; **18**:065015.
44. Bathe KJ. *Finite Element Procedures*. Prentice-Hall, MIT: Massachusetts, U.S.A., 1996.
45. Liu GR, Quek SS. *The Finite Element Method*: *A Practical Course*. Butterworth Heinemann: Oxford, 2003.
46. Zhang Z. Recovery techniques in finite element methods. In *Adaptive Computations*, Chapter 8. Tang T, Xu J (eds). Mathematics Monograph Series, vol. 6. Science Publisher: Beijing, 2007.
47. Carstensen C. Reliable and efficient averaging techniques as universal tool for a posteriori finite element error control on unstructured grids. *International Journal of Numerical Analysis and Modeling* 2006; **3**:333–347.

48. Dorfler W. A convergent adaptive algorithm for Poisson's equation. *SIAM Journal on Numerical Analysis* 1996; **33**:1106–1124.
49. Chen L. Short implementation of bisection in MATLAB. In *Recent Advances in Computational Sciences—Selected Papers from the International Workship on Computational Sciences and its Education*, Jorgensen P, Shen X, Shu C-W, Yan N (eds). World Scientific Press: Beijing, 2008; 318–332.
50. Funken S, Praetorius D, Wissgott P. Efficient implementation of adaptive p1-FEM in Matlab, Preprint 2008. Available from: www.asc.tuwien.ac.at/preprint/2008/asc19x2008.
51. Timoshenko SP, Goodier JN. *Theory of Elasticity* (3rd edn). McGraw-Hill: New York, 1970.
52. Hung N-X, Stéphane B, Hung N-D. Smooth finite element methods: convergence, accuracy and properties. *International Journal for Numerical Methods in Engineering* 2008; **74**:175–208.
53. Richardson LF. The approximate arithmetical solution by finite differences of physical problems. *Transactions of the Royal Society* (*London*) 1910; **A210**:307–357.
54. Fraeijs de Veubeke BM. Displacement and equilibrium models in the finite element method. In *Stress Analysis*, Zienkiewicz OC (ed.). Wiley: London, 1965.
55. Beckers P, Zhong HG, Maunder E. Numerical comparison of several a posteriori error estimators for 2D stress analysis. *European Journal of Finite Element Method* 1993; **1**:165–178.
56. Debongnie JF, Zhong HG, Beckers P. Dual analysis with general boundary conditions. *Computer Methods in Applied Mechanics and Engineering* 1995; **122**:183–192.
57. Bordas S, Duflot M. Derivative recovery and a posteriori error estimate for extended finite elements. *Computer Methods in Applied Mechanics and Engineering* 2007; **196**:3381–3399.
58. Waisman H, Belytschko T. Parametric enrichment adaptivity by the extended finite element method. *International Journal for Numerical Methods in Engineering* 2008; **73**:1671–1692.

DOI: 10.1002/cnm